Proceedings of ALGORITMY 2009
pp. 331–340

SIMULATING CERTAIN ASPECTS OF MULTIPHASE FLOW USING STOCHASTIC DIFFERENTIAL EQUATIONS

DAVID W. DEAN*

Abstract. Modifications to a stochastic differential equation (SDE) approach for modeling single and two phase NAPL flow are proposed which are intended to allow SDE modeling of the motion of air bubbles in porous media. Bubble flow and channeling are discussed along with bubble sticking, bubble coalescing, bubble breakup and air sparging.

Key words. stochastic differential equations, two-phase flow, bubble motion

AMS subject classifications. 34F05, 60H05, 60H10, 60H35, 86A05

1. Background. In previously presented work, ideas involving stochastic differential equations (SDE's) were used to model single and two-phase flow of NAPL in a water saturated porous media, Dean *et al.* [4], [5]. This approach results in a nonlinear SDE that describes the position of the NAPL fluid particles. The control of NAPL fluid particles across a permeability interface, pooling, is accomplished using a jump term which derives from the Itô formula for càdlàg semimartingales Dean *et al.* [6],[7], Kloeden and Platen [14], Protter [18], and is based on capillary diffusivity and the pressure-saturation curves of the sands forming the interface.

1.1. Stochastic Differential Equation Model. Consider an m-dimensional Wiener process $\vec{W} = \{\vec{W}_t : t \geq 0\}$ with components $\vec{W}_t = \left[W_t^1, W_t^2, \cdots, W_t^m\right]^{\mathsf{T}}$ which are independent scalar Wiener processes with respect to a common family of σ-algebras $\{\mathcal{A}_t : t \geq 0\}$. Let $\vec{a}(t, \vec{x})$ be a d-dimensional vector function such that $\vec{a} : [0, T] \times \Re^d \to \Re^d$, $T \geq 0$ and let $\mathbf{B}$ be a $d \times m$-matrix function such that $\mathbf{B} : [0, T] \times \Re^d \to \Re^{d \times m}$. These form the vector SDE

$$d\vec{X}_t = \vec{a}(t, \vec{X}_t)\, dt + \mathbf{B}(t, \vec{X}_t)\, d\vec{W}_t, \tag{1.1}$$

which is interpreted as $\vec{X} = \vec{X}_0 + \int_0^t \vec{a}(s, \vec{X}_s)ds + \int_0^t \mathbf{B}(s, \vec{X}_s)d\vec{W}_s$. Using Itô's lemma, the conditional probability density of a particle $\vec{X}_p$ starting at $(\vec{x}_0, t_0)$, $p(\vec{x}, t) \equiv p(\vec{x}, t; \vec{x}_0, t_0)$ is given by

$$\frac{\partial p(\vec{x}, t)}{\partial t} + \nabla \cdot \left[\left(\vec{a}(t, \vec{x}) - \nabla^{\mathsf{T}}\mathbf{D}^{\mathsf{T}}(t, \vec{x})\right) p(\vec{x}, t)\right] - \nabla \cdot \mathbf{D}(t, \vec{x}) \nabla p(\vec{x}, t) = 0, \tag{1.2}$$

where $2\mathbf{D} = \mathbf{B}\mathbf{B}^{\mathsf{T}}$, which illustrates the relationship between the SDE and the PDE.

1.2. Two-Phase Flow. The type of problem to be modeled is the contamination of groundwater by a non-wetting fluid such as a NAPL. The laboratory experiments used Soltrol, which is lighter than water, or an LNAPL. The continuity equation and Darcy's law are used to develop a Fokker-Planck equation for the non-wetting phase, S_n, which has the form

*Colorado School Of Mines (ddean@mines.edu).

$$\frac{\partial S_n}{\partial t} + \nabla \cdot \left[\frac{1}{\theta_n} \left(f_n \vec{q}_t - \bar{\lambda}\gamma_w \mathbf{k}\vec{z} + \bar{\lambda}\gamma_n \mathbf{k}\vec{z} \right) S_n \right] - \nabla \cdot \left(\frac{\bar{\lambda}\mathbf{k}}{\phi} \frac{dp_c}{dS_n} \right) \nabla S_n = 0, \tag{1.3}$$

where in this equation, γ_α is the specific weight of the α-phase, $\bar{\lambda} = \frac{\lambda_w \lambda_n}{\lambda_w + \lambda_n}$, $f_n = \frac{\lambda_n}{\lambda_w + \lambda_n}$, $\lambda_\alpha = \frac{k_{r\alpha}}{\mu_\alpha}$, $\vec{z} = (0, 0, -1)^\mathsf{T}$, μ_α is the viscosity of the α-phase, $k_{r\alpha}$ is the relative permeability of the α-phase, p_c is the capillary pressure, θ is volumetric fraction, ϕ is the porosity, $\mathbf{k}$ is the intrinsic permeability and $\vec{q}_t$ is the total velocity. Letting $\mathbf{D} = \frac{\bar{\lambda}\mathbf{k}}{\phi} \frac{dp_c}{dS_n} = \frac{1}{2}\mathbf{B}\mathbf{B}^\mathsf{T}$, the associated SDE, Dean [6], is

$$d\vec{X}_t = \left(\frac{1}{\theta_n} \left(\bar{\lambda}\gamma_n \mathbf{k}\vec{z} - \bar{\lambda}\gamma_w \mathbf{k}\vec{z} + f_n \vec{q}_t \right) + \nabla^\mathsf{T} \mathbf{D}^\mathsf{T}(t, \vec{X}_t) \right) dt + \mathbf{B}(t, \vec{X}_t)\, d\vec{W}_t.$$

Figure 1.1 shows how the model simulates pooling and channeling when an LNAPL plume encounters a broken lens of low permeability. Figure 2.1A illustrates how the model simulates fingering through an interface between coarse and fine sands.

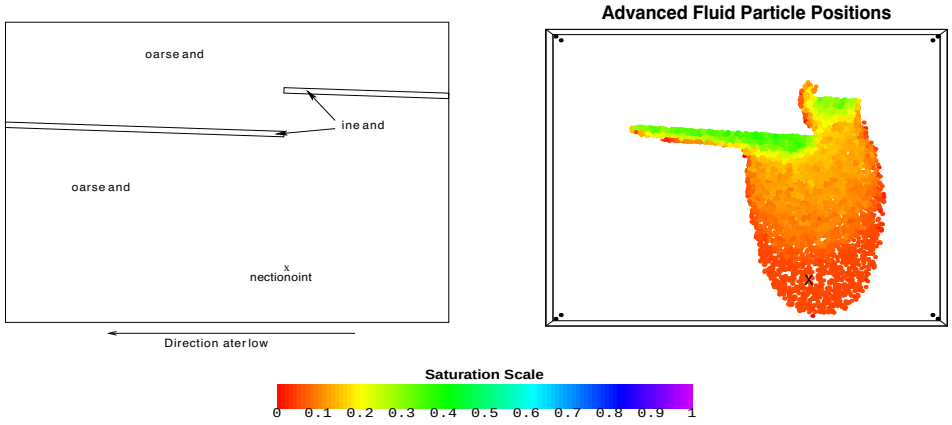

FIG. 1.1. *NAPL Pooling And Channeling*

1.3. Computational SDE. As in the case of deterministic differential equations, many different time discrete approximations exist. In order to compare different discrete approximations, *the rates of weak convergence* can be used - see Kloeden and Platen [14] for details.

In our case, we are interested in numerically solving the d-dimensional stochastic differential equation whose k^{th} component is given by

$$\vec{X}_t^k = \vec{X}_{t_0}^k + \int_{t_0}^t \vec{a}^k(s, \vec{X}_s)\, ds + \sum_{j=1}^m \int_{t_0}^t \mathbf{B}^{k,j}(s, \vec{X}_s)\, d\vec{W}_s^j,$$

where $t \in [t_0, T]$. The Itô-Taylor expansion can be used to specify approximation methods for $\vec{X}_t$. This expansion has the form

$$f(\tau, \vec{X}_\tau) = \sum_{\alpha \in \mathcal{A}} I_\alpha \left[f_\alpha(\rho, \vec{X}_\rho) \right]_{\rho,\tau} + \sum_{\alpha \in \mathcal{B}(\mathcal{A})} I_\alpha \left[f_\alpha(\cdot, \vec{X}_\cdot) \right]_{\rho,\tau}, \tag{1.4}$$

where $\rho(\omega)$ and $\tau(\omega)$ are stopping times such that

$$t_0 \leq \rho(\omega) \leq \tau(\omega) \leq T \qquad \text{w.p. 1,}$$

the I_α are multiple Itô integrals, $\mathcal{A}$ is a hierarchical set and $\mathcal{B}(\mathcal{A})$ is its remainder and the f_α are the Itô coefficient functions, see Kloeden and Platen [14], chapter 5 for the details. The simplest weak Itô-Taylor approximation scheme is given by

$$\vec{Y}^k_{n+1} = \sum_{\alpha\in\mathcal{A}} \vec{f}^k_\alpha(\tau_n, \vec{Y}_n) I_{\alpha,\tau_n,\tau_{n+1}} = \vec{Y}^k_n + \vec{a}^k(\tau_n, \vec{Y}_n)\Delta_n + \sum_{j=1}^{m} \mathbf{B}^{k,j}(\tau_n, \vec{Y}_n)\Delta W^j_n$$

which is known as the *Euler scheme*. Under sufficient assumptions, it can be shown that this approximation scheme has a weak order of convergence of $\beta = 1$, Kloeden and Platen [14]. Higher order schemes can be similarly derived by including higher order Itô integrals from the Itô-Taylor expansion.

Although the Itô-Taylor expansion can be used to establish numerical schemes in uniform sands, the methods must be modified to simulate anisotropic dispersion, pore scale fingering and pooling at interfaces of sands of different permeabilities, Dean *et al.* [6], [7].

2. Types Of Bubble Flow. As guides to the bubble flow patterns discussed in the in situ air sparging (ISAS) techniques, we will use Ji *et al.* [11] and Brooks *et al.* [2]. In some cases, the flow pattern descriptions are not always clear. For example, Brooks *et al.* [2] uses channel flow, slug flow, mixed pattern, mixed flow and bubble flow. However, they do identify two general patterns on which we will focus - channel flow and bubble flow. As a general rule, they conclude that "$\cdots$ ISAS in a porous media characterized by medium sand or smaller will have air channels, while the flow pattern in porous media composed of coarse sand or larger will have bubble flow."

2.1. Channel Flow. According to Brooks *et al.* [2], in channel flow the air displaces water along continuous paths. Again, there seems to be some flexibility in the interpretation of what this actually means. Two extremes of this pattern are:

1. "$\cdots$ a macro scale, dendritic (tree branch) distribution of air channels of limited cross-sectional extent, originating from the point of air injection $\cdots$"
2. "$\cdots$ an air distribution in which the air saturation varies continuously over the entire domain influenced by the air injection point."

In their experimental results section, they offer the following; "Channel flow was used to describe the pattern when areas within the column suddenly desaturated and remained significantly unsaturated for the duration of the applied pressure. Bubble flow and slug flow were used to describe the patterns characterized by moving bubbles or moving slugs, respectively. The distinction between bubbles/slugs and channels was not always clear. In general, if an area was not significantly resaturated after initial desaturation, then the pattern was labeled channel flow. Mixed flow was used when it appeared that a combination of either bubbles or slugs and channels were present."

Figure 2.1B is the result of applying the model to create a channelized flow. It seems to fit somewhere into the numerous possibilities of what channelized flow can be. Basically, we start with a tank packed with a uniform sand and then form in the tank the four high permeability channels shown in color in the figure. The bubbles are shown in black. This is consistent with Brooks' *et al.* [2] characterization of channel flow "$\cdots$ in which air displaces liquid along continuous paths of least resistance." The

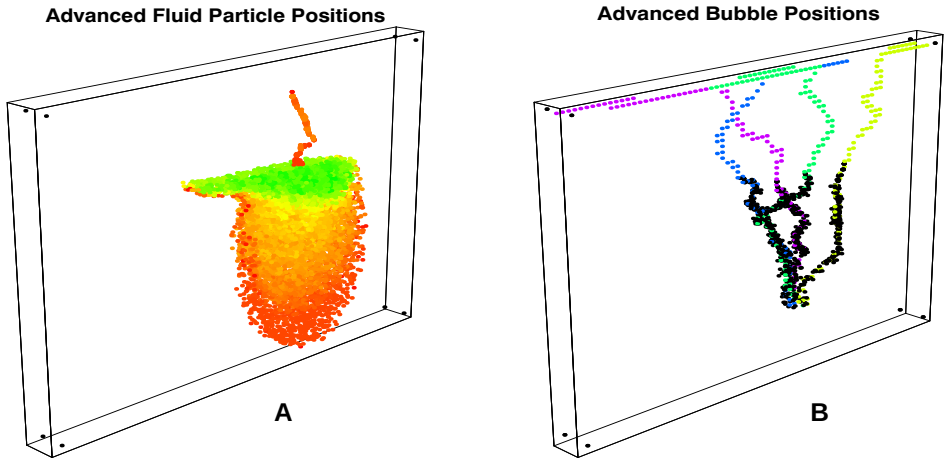

FIG. 2.1. *NAPL Fingering And Air Bubble Channels*

dendritic nature of the channels is evident as well as their limited cross-sectional extent and their origin at the point of air injection. The channeling algorithm originated with our attempts to simulate NAPL fingering at coarse/fine sand interfaces in two-phase flow. As with bubble flow, the channel flow model tries to take into consideration bubble sticking, bubble coalescence and bubble breakup. Since the same algorithms are used in both cases, they will be discussed below.

2.2. Bubble Flow. The other type of bubble movement we are considering is sometimes called bubbly flow or just bubble flow. It should be noted that the terminology used to characterize these flows in the literature seems to be dependent on the interpretation of the author. In our case, what is meant by bubbly flow or bubble flow is a flow of bubbles that (very) generally trace out an elliptic paraboloid in a 3-dimensional space of uniform material. However, in a heterogeneous environment, the bubbles tend to behave in a manner similar to NAPL flow. We will illustrate this later.

Appealing to Newton's second law, we have

$$\vec{F} = m\vec{a} = m\frac{d\vec{v}}{dt},$$

so that

$$\int_0^t \vec{F}(s)\, ds = \int_0^t m\, d\vec{v}(s) = m\vec{v}(t).$$

In Dean [6], see also Honerkamp [9], it is shown that the diffusion process $\vec{X}(t)$ whose probability density satisfies the Fokker-Planck equation also satisfies the SDE

$$d\vec{X}_t = \vec{a}(t, \vec{X}_t)\, dt + \mathbf{B}(t, \vec{X}_t)\, d\vec{W}_t,$$

where $d\vec{W}_t$ is a white noise process such that $d\vec{W}(t) = \vec{\eta}\sqrt{(}dt)$ and $\vec{\eta}$ is a vector of standard normal variables. This equation is a Langevin equation which describes an Ornstein-Uhlenbeck process.

The model that we are using to describe the bubble movement is given by

$$\vec{X}_t = \vec{X}_0 + \int_0^t \left(\frac{1}{\theta_n} \left(\hat{\lambda}\gamma_n \mathbf{k}\vec{z} - \hat{\lambda}\gamma_w \mathbf{k}\vec{z} \right) \right) \, ds + \int_0^t \mathbf{B}(s, \vec{X}_s) \, d\vec{W}_s. \tag{2.1}$$

The integrand in the first integral on the RHS of Equation(2.1) is a velocity and $\mathbf{B}(s, \vec{X}_s)$ in the integrand of the second integral on the RHS of Equation(2.1) is derived from the diffusion coefficient, $\mathbf{D}$, using the relationship $\mathbf{D} = \frac{1}{2}\mathbf{B}\mathbf{B}^{\mathsf{T}}$. Since the dimension of $\mathbf{D}$ is $\frac{l^2}{t}$, the dimension of $\mathbf{B}$ is $\frac{l}{\sqrt{(t)}}$ and since the dimension of $d\vec{W}_s$ is $\sqrt{(t)}$ the second integral on the RHS of Equation(2.1) is also a distance. Generally speaking, $\mathbf{B}$ plays the role of a velocity. The second integral on the RHS of Equation(2.1) is an Itô integral and not the usual Stieltjes integral. Conceptually, the time derivative of $\vec{X}_t$ is a velocity and the impulse force is then the mass times this velocity.

Let

$$F_B \vec{D}_g = \hat{\lambda} \left(\gamma_n - \gamma_w \right) \mathbf{k}\vec{z} = \frac{\psi}{\mu} \left(\gamma_n - \gamma_w \right) \mathbf{k}\vec{z} \equiv \frac{V_B}{\mu} \left(\rho_n - \rho_w \right) g \mathbf{k}\vec{z}, \tag{2.2}$$

where ψ is a dimensionless scaling factor whose magnitude is equal to the volume V_B. In this model, the forces determining the motion of an air bubble, B, in a saturated porous media consist of the buoyancy force, the drag force and the surface tension force. In Equation(2.2), the buoyancy force is represented by

$$F_B = V_B \left(\rho_n - \rho_w \right) g,$$

and the drag force is represented by

$$\vec{D}_g = \frac{1}{\mu} \mathbf{k}\vec{z}.$$

Since $\vec{z} = (0, 0, -1)^{\mathsf{T}}$, $\hat{\lambda} \left(\gamma_n - \gamma_w \right) \mathbf{k}\vec{z} \geq 0$. The permeability of the sand, $\mathbf{k}$, is related to drag, Bear [1]. Also, the greater the viscosity of the fluid, the slower the bubble will move, hence the inverse relationship. The surface tension around a spherical pore throat, assuming a zero contact angle, is given by

$$F_s = 2\pi r \sigma \text{ where } \sigma = 72.86 \pm 0.05 \, dyne/cm \text{ at } 20^\circ \, C.$$

The buoyancy force and the drag force are represented in Equation(2.2). The effect of the surface tension force is applied on a time step by time step and bubble by bubble basis.

2.3. Bubble Sticking, Coalescence and Breakup. At each time step, the bubble is facing a pore throat whose size is determined by sampling from the grain size distribution and converting the selected grain size to an equivalent pore size, Dean [6], [7]. If the size of the bubble is less than the pore size, the bubble is allowed to pass through the pore throat. If the size of the bubble is greater than or equal to the pore throat, then

1. If $F_B \vec{D}_{g,i} > F_s$, the bubble is allowed to pass.
2. If $F_B \vec{D}_{g,i} \leq F_s$, the bubble is stuck.

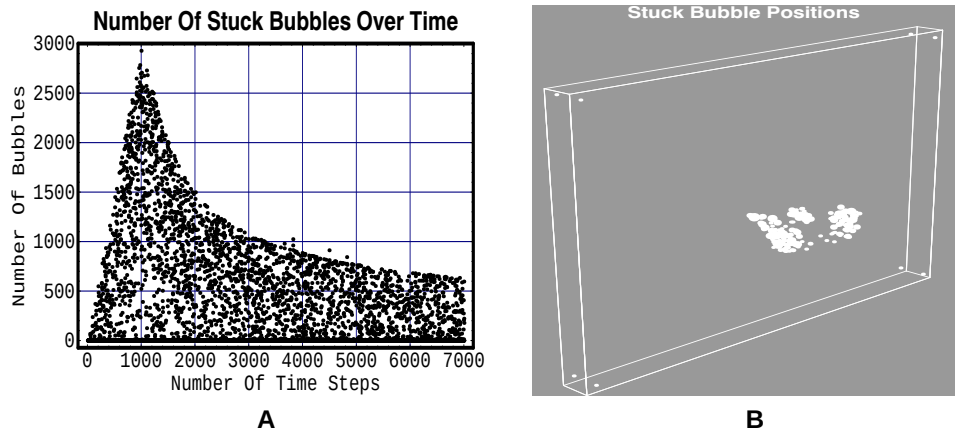

FIG. 2.2. *Bubbles Stuck Over Time*

It turns out that in this model, the bubble sticking phenomenon is a very dynamic process. This is illustrated in Figure 2.2A, which is a very busy graph. In this experiment, 3000 bubbles of radius $0.1cm$ were injected uniformly over 1000 time steps, i.e., 3 bubbles each time step. The total length of the experiment was 7000 time steps. Figure 2.2 shows the total number of bubbles that were stuck at the end of each time step. If this is reflective of reality, then the flow of bubbles would be greatly influenced by the sticking of bubbles. Figure 2.2B shows the position and size of the bubbles stuck at the end of the experiment.

There are some processes that it seems likely would tend to release a stuck bubble, either partially or completely from its imprisonment. First, and probably the most questionable, is at each time step the pore throat size is randomly changed. The reason for this is that the positions of the grains of sand can be changed by movement of the water or the impact of other bubbles in the region near the stuck bubble. Secondly, other bubbles might come along and coalesce with the stuck bubble thereby increasing its buoyancy to the point where the force holding the bubble is overcome. Thirdly, a snap-off mechanism might release a portion of the bubble from its captivity and keep the remainder entrapped.

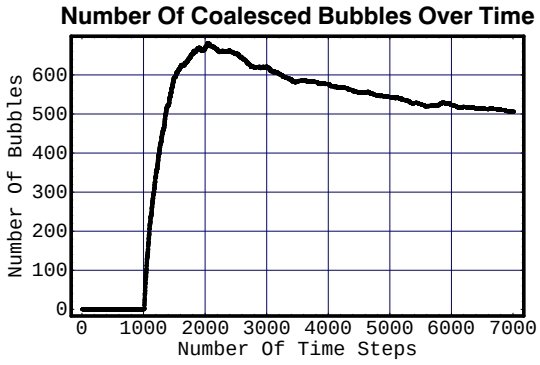

FIG. 2.3. *Bubbles Coalesced Over Time*

Two bubbles might also coalesce if they come in contact with each other. In theory, when two air bubbles come close together, a water film forms between them. As the water in the film between them drains, if it does, it will ultimately reach a critical thickness at which the film ruptures and the bubbles coalesce. Kim and Lee [12] give an estimate of this final film thickness to be $1 \times 10^{-6} cm$. Some estimates for time to coalescence are in the range of $10^{-3} - 10^{-4} sec$, Prince and Blanch [17], Marrucci [16]. These results do depend on some simplfying assumptions. But, in light of these results, our algorithm for coalescence depends on the assumption that when there is contact between a stuck bubble and a free bubble, then coalescence occurs. The stuck bubble increases in size and the free bubble disappears. If the buoyancy of the stuck bubble increases enough due to its increase in volume to overcome the surface tension force at the pore throat, then the stuck bubble will become unstuck.

Figure 2.3 shows the number of coalesced bubbles at the end of each time step. The flat line from $0 - 1000$ is self-imposed. It is intended to cover the injection zone where it is possible that chaotic conditions could be occurring. In other words, a lot of bubbles would be competing for space in a very limited volume. So, it is assumed that bubble coalescence and bubble breakup would be cancelling each other out. Suffice it to say that more work has to be done to realistically simulate this part of the bubble flow.

As mentioned above, bubble breakup is also a dynamic force at play in determining the distribution of bubbles over time. Although several bubble breakup mechanisms have been suggested in the literature, Javadpour [10], the mechanism we have chosen is a form of snap-off. In theory, Kovscek and Radke [15], as with bubble coalescence, bubble breakup has to do with the liquid film at the pore throat. The sequence of events seems to be

1. Air bubble enters a liquid pore throat
2. Water accumulates at the pore throat into a collar isolating a portion of the air bubble
3. The water eventually forms a lens that spans the pore throat thus separating the isolated portion of the air bubble
4. The lens separates from the pore throat separating the isolated portion as a separate air bubble

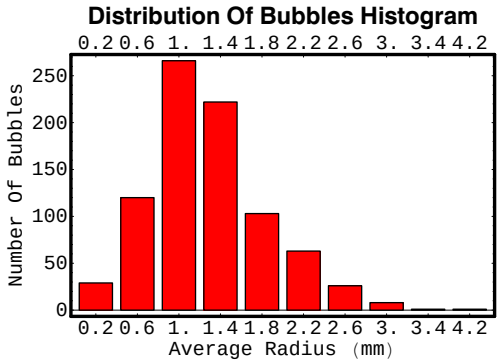

FIG. 2.4. *Distribution Of Bubbles By Size*

The algorithm used to simulate bubble breakup follows this prescription. Generally, as the bubble attempts to pass through the pore throat if a portion of the bubble is such that

$$F_B \vec{D}_{g,i} > F_s$$

then that portion of the bubble is allowed to separate and exist as a separate bubble. Figure 2.4 shows the distribution of bubbles by size at the end of the experiment. As before, the 3000 bubbles originally injected all had a radius of $0.1cm$. As shown in Figure 2.4, at the end of the experiment the largest number of remaining bubbles still have a radius of $0.1cm$, but some of the bubbles are smaller, due to breakup, and some are larger, due to coalescence.

Figure 2.5 shows two views of bubble flow around two impervious lenses. The bubble flow plumes shown in this figure are the result of numerical experiments similar to actual bubble flow experiments conducted by Ji *et al.* [11] who used glass beads as the porous medium. The implication for air sparging is that if the contaminant is above the impervious lens, then the bubbles will likely not reach it. Also, the horizontal spreading of the air bubbles beneath the impervious layer may cause the contaminant plume to spread in the horizontal directions.

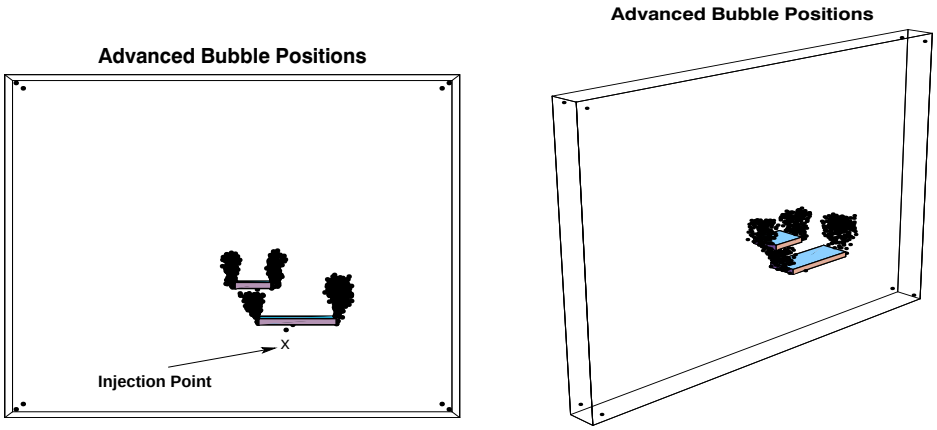

FIG. 2.5. *Bubble Flow Around Impervious Lenses*

2.4. Air Sparging. Figures 2.6 and 2.7 are intended to illustrate this type of bubble behavior. The context of these illustrations is one of air sparging. In Figure 2.6, a residual NAPL plume is shown which is assumed to be immobile. The saturation of the plume is low, varying between 0% and 3.6% as indicated by the associated Percent Saturation Scale.

Also shown in Figure 2.6 are the injection points where the air is injected below the stationary NAPL plume. As time progresses, the air bubbles rise up, fan out and pass through the residual NAPL. Figure 2.7 shows the progress of the air bubbles as they pass the halfway point of the tank.

As the flow of bubbles of air passes through the experimental tank, the individual air bubbles interact with the residual NAPL plume and a part of the volatile NAPL is transferred to the air bubbles and carried off. This is shown, in an exaggerated sense, by the NAPL plume changing from a reddish color to a grayer color. The tracks are clearly visible in the two images shown in Figure 2.7.

The algorithm keeps track of the positions of the NAPL particles and the mass of NAPL associated with them. As the bubble moves, if it encounters a NAPL particle,

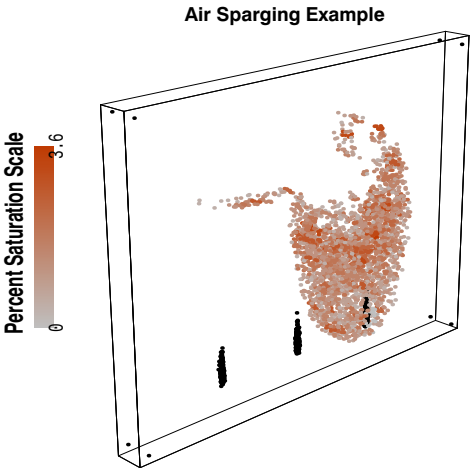

FIG. 2.6. *Distribution Of NAPL And Initial Bubble Flow*

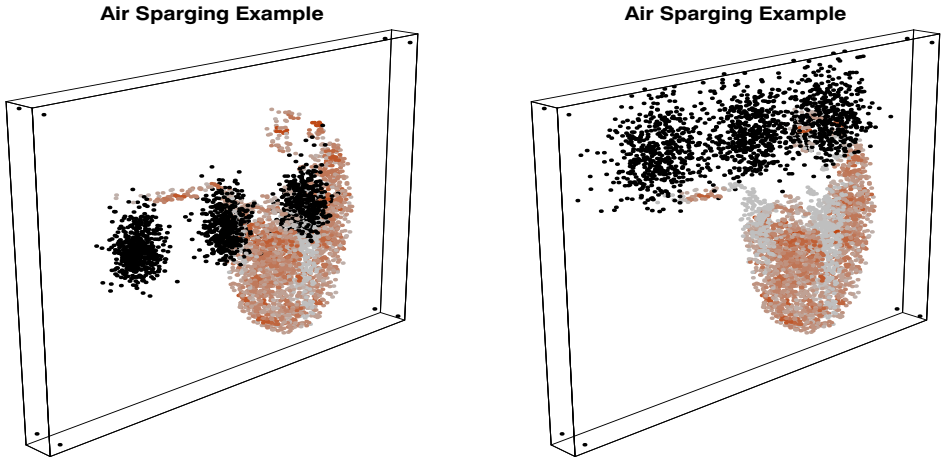

FIG. 2.7. *Effect Of Air Sparging*

i.e., the NAPL particle falls within the spherical volume of the air bubble, then a percentage of the mass associated with the NAPL particle is transferred to the air bubble and carried off. When the NAPL saturations are recomputed, this loss of mass is recorded as a change in color from more reddish to more grayish. In Figure 2.7, the air bubbles are ready to leave the tank, and their tracks through the NAPL plume are evident when compared to the relatively undisturbed NAPL plume shown in Figure 2.6.

The program that generated these images is still very much under development and will no doubt undergo many changes in the future. However, this is pretty much what we have at the present. Since we have very little in the way of our own experimental results to use for scaling and validating these results, we have had to use our own judgement in developing them. Since we cannot look into the inside of a three dimensional domain to observe the movement of the individual bubbles, more results such as those reported in Chen *et al.* [3], where Xray tomography was used to

produce images of air distribution patterns, are needed.

REFERENCES

[1] Bear, Jacob, *Dynamics of fluids in porous media*, Dover, 1972

[2] Michael C. Brooks, William R. Rise and Michael D. Annable, Fundamental Changes in In Situ Air Sparging Flow Patterns, *Ground Water Monitoring and Remediation*, spring 1999, pp. 105-113

[3] May-Ru Chen, Richard E. Hinkley and John E. Killough, Computed tomography imaging of air sparging in porous media, *Water Resources Research*, 32(10), pp 3013-3024, Oct, 1996

[4] Dean, D.W. and Russell, T.F., *A numerical Lagrangian stochastic approach to upscaling of dispersivity in solute transport*, Advances in Water Resources, 27(2004)

[5] Dean, D.W., Russell, T.F., Illangasekare, T.H., Using stochastic differential equations in modeling NAPL flow in heterogeneous porous media, *MODFLOW and More 2006: Managing Groundwater Systems*, Conference Proceedings, Vol 1, pp. 347, May, 2006

[6] Dean, D.W., *Final Report - DMS 0222300*, National Science Foundation, Feb, 2007

[7] Dean, D.W., *Final Report - DMS 0222286*, National Science Foundation, Sep, 2007

[8] Hinchee, Robert E., Editor, *Air Sparging for Site Remediation*, CRC Press, 1994

[9] Honerkamp, J., *Statistical Physics*, Springer, 1998

[10] Javadpour, F., Bubble Breakup in Porous Media, *Journal of Canadian Petroleum Technology*, 46(8), August, 2007

[11] Wei Ji, Amine Dahmani, David P. Ahlfeld, Jia Ding Lin, Edward Hill III, Laboratory Study of Air Sparging: Air Flow Visualization, *Ground Water Modeling and Remediation*, pp. 115-126, Fall 1993

[12] Kim, W.K. and Lee, K.L., Coalescence Behavior of Two Bubbles in Stagnant Liquids, *J. of Chem. Eng. of Japan*, 20, page 449, 1987

[13] Kirkpatrick, R.D. and Lockett, M.J., The Influence of Approach Velocity on Bubble Coalescence, *Chem. Eng. Sci.*, 29, page 2363, 1974

[14] Kloeden, Peter E. and Platen, Eckhard, *Numerical Solution of Stochastic Differential Equations*, Springer, 1992

[15] Kovscek, A. R. and Radke, C. J., Gas bubble snap-off under pressure-driven flow in constricted noncircular capillaries, *Colloids Surfaces A: Physicochem. Eng. Aspects 117*, pp. 55-76, 1996

[16] Marrucci, G., A theory of coalescence, *Chem. Eng. Sci.*, 24, page 975, 1969

[17] Prince, Michael J. and Blanch, Harvey W., Bubble Coalescence and Break-Up in Air-Sparged Bubble Columns, *AIChE Journal*, Vol. 36(10), pp. 1485-1499, Oct, 1990

[18] Protter, Philip, *Stochastic Integration and Differential Equations*, 2^{nd} Edition, Springer-Verlag, 2004